nature materials

Letter

https://doi.org/10.1038/s41563-023-01478-4

Proximity-induced superconductivity in epitaxial topological insulator/graphene/gallium heterostructures

Received: 29 April 2022

Accepted: 12 January 2023

Published online: 13 February 2023



Cequn Li¹, Yi-Fan Zhao ®¹, Alexander Vera^{2,3}, Omri Lesser ®⁴, Hemian Yi¹, Shalini Kumari^{2,3}, Zijie Yan ®¹, Chengye Dong⁵, Timothy Bowen^{2,3}, Ke Wang⁶, Haiying Wang⁶, Jessica L. Thompson⁷, Kenji Watanabe ®⁸, Takashi Taniguchi ®⁹, Danielle Reifsnyder Hickey ®^{3,6,7}, Yuval Oreg ®⁴, Joshua A. Robinson^{1,2,3,5,6,7}, Cui-Zu Chang ®¹ & Jun Zhu ®^{1,2,5} \subseteq

The introduction of superconductivity to the Dirac surface states of a topological insulator leads to a topological superconductor, which may support topological quantum computing through Majorana zero modes^{1,2}. The development of a scalable material platform is key to the realization of topological quantum computing^{3,4}. Here we report on the growth and properties of high-quality (Bi,Sb)₂Te₃/graphene/gallium heterostructures. Our synthetic approach enables atomically sharp layers at both hetero-interfaces, which in turn promotes proximity-induced superconductivity that originates in the gallium film. A lithography-free, van der Waals tunnel junction is developed to perform transport tunnelling spectroscopy. We find a robust, proximity-induced superconducting gap formed in the Dirac surface states in 5–10 quintuple-layer (Bi,Sb)₂Te₃/ graphene/gallium heterostructures. The presence of a single Abrikosov vortex, where the Majorana zero modes are expected to reside, manifests in discrete conductance changes. The present material platform opens up opportunities for understanding and harnessing the application potential of topological superconductivity.

A primary approach to realize topological superconductivity in a potentially scalable material platform is to exploit the superconducting proximity effect of a hybrid system involving an s-wave superconductor (SC), and a one-dimentional (1D) or two-dimensional (2D) semiconductor with strong spin–orbit coupling $^{3-5}$. Studies following this approach have made much progress in fundamental science and materials engineering but have also encountered great challenges 4 . As envisioned by Fu

and Kane 1 , topological superconductivity is also predicted to occur in a hybrid system of a topological insulator (TI) and SC, where the lifting of the spin degeneracy, a key ingredient for topological superconductivity, is already achieved in the helical surface states of a topological insulator. Scanning tunnelling microscopy studies have reported proximity-induced superconductivity and signatures of Majorana zero modes in TI/SC heterostructures $^{6-9}$. However, the difficulty of creating

¹Department of Physics, The Pennsylvania State University, University Park, PA, USA. ²Center for 2-Dimensional and Layered Materials, The Pennsylvania State University, University Park, PA, USA. ³Department of Materials Science and Engineering, The Pennsylvania State University, University Park, PA, USA. ⁴Department of Condensed Matter Physics, Weizmann Institute of Science, Rehovot, Israel. ⁵2-Dimensional Crystal Consortium, The Pennsylvania State University, University Park, PA, USA. ⁶Materials Research Institute, The Pennsylvania State University, University Park, PA, USA. ⁷Department of Chemistry, The Pennsylvania State University, Univers

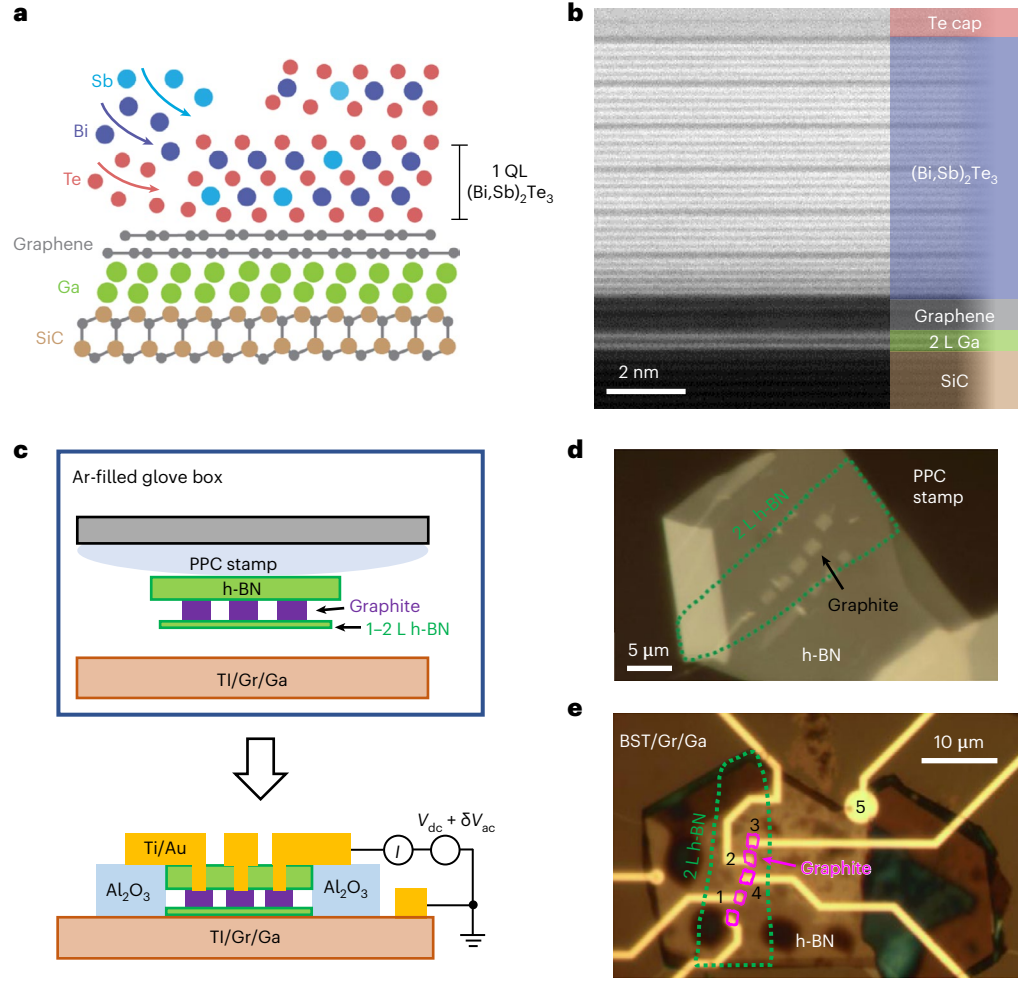


Fig. 1|Epitaxial growth of BST/Gr/Ga heterostructures and fabrication of tunnel junction devices. a, Schematic of the growth, combining CHet growth of Gr/2 L-Ga and MBE growth of (Bi,Sb)₂Te₃. b, A cross-sectional STEM image showing the atomically sharp hetero-interfaces between 6 QL (Bi,Sb)₂Te₃, epi-graphene and the 2 L Ga. c, Schematics of the van der Waals tunnel junction construction, device structure and the differential tunnelling conductance measurement set-up where a d.c. voltage (V_{dc}) with a small a.c. modulation (δV_{ac})

is applied to the graphite electrode. **d**, Optical image of an h-BN/graphite/2 L-h-BN stack on a poly(propylene) carbonate (PPC) stamp. The graphite squares are produced by atomic force microscope oxidation nanolithography 33 and are $^{-3}\,\mu\text{m}^2$ in area. **e**, Optical image of device 02T-SQL with four tunnel junctions as labelled. Contacts 1–4 are made to the graphite electrodes, and contact 5 directly contacts the BST/Gr/Ga film.

high-quality, scalable platforms remains a major roadblock to further experimentation. A high-quality TI film can be grown on bulk NbSe $_2$ (refs. $^{6-8}$), but does not form a clean hetero-junction on metallic film SCs such as Al or Nb due to interfacial reactions 10 . In addition, preventing the oxidization of TI films is a challenge in device fabrication. Transport studies, a major experimental probe of Majorana zero modes, remain limited in TI/SC heterostructures $^{11-14}$.

In this work, we demonstrate the synthesis of epitaxial (Bi,Sb) $_2$ Te $_3$ /graphene/gallium (BST/Gr/Ga) thin films with atomically sharp hetero-interfaces. We construct clean van der Waals tunnel junctions and employ transport tunnelling spectroscopy to probe their superconducting properties. Tunnelling spectra obtained on heterostructures with a BST thickness ranging from 5 to 10 quintuple layers (QLs) exhibit the characteristics of two superconducting gaps. The larger gap originates from the superconducting Ga film 15 . We attribute the smaller gap, which is 30–50% of the gap in Ga, to proximity-induced superconductivity in the Dirac surface states of the BST film. The introduction of magnetic vortices leads to discrete tunnelling conductance jumps, with the smallest unit corresponding to the increment of a single flux quantum. Our experiments established a large-area, potentially

scalable TI/SC platform for studies of topological superconductivity and Majorana physics.

As illustrated in Fig. 1a, BST/Gr/Ga heterostructures are synthesized in two steps. We intercalate an atomically thin 2D Ga film at epi-graphene/6H-SiC(0001) substrates using confinement heteroepitaxy (CHet) $^{\rm 15}$. The Ga film covers 90% of the wafer, grows uniformly and epitaxially across the majority of the terraces of the SiC substrate and consists of mainly two-atomic-layer-thick (2 L) Ga, although 1 L and 3 L Ga are also present in some regions of the wafer $^{\rm 16,17}$. The 2D Ga films exhibit superconductivity with a transition temperature of approximately 3–4 K, higher than that of the bulk α -Ga (ref. $^{\rm 18}$), which is attributed to electron–phonon interactions and the free-electron-like pockets near the Ga K points. A full characterization and understanding of the growth and superconductivity of 2D Ga is given in the references $^{\rm 15-17}$.

We then grow $(Bi,Sb)_2Te_3$ of controlled thickness and composition using molecular beam epitaxy $(MBE)^{19}$. Crucially, the epi-graphene layer acts as a chemical barrier to prevent the formation of Ga-(Bi,Sb) alloys and a Ga-Te compound, and templates the growth of BST due to their similar lattice structures 20,21 . This approach results in abrupt,

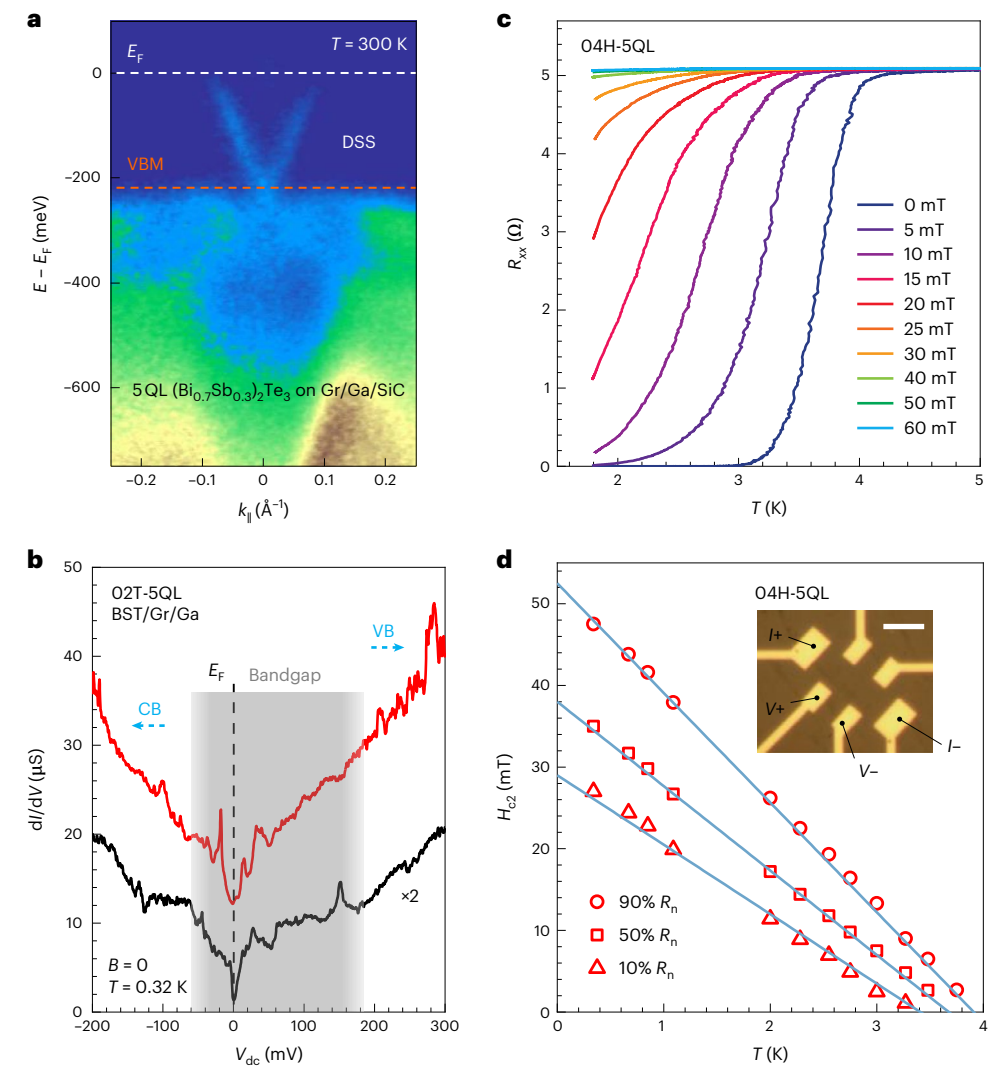


Fig. 2 | Coexistence of Dirac surface states and superconductivity in BST/Gr/Ga heterostructures. a, Room-temperature ARPES band map of a 5 QL $(Bi_{0.7}Sb_{0.3})_2Te_3/Gr/Ga$ film. k_{\parallel} , in-plane momentum. DSS, Dirac surface states; VBM, valence band maximum. b, The dI/dV versus V_{dc} curves obtained on 02T-5QL, made on the same film as in a. Red and black curves are from different junctions. The red curve is shifted vertically by 10 μS for clarity. A positive d.c. bias probes states below the Fermi level. The grey shaded box corresponds to the bulk bandgap region of the BST film, consistent with the ARPES measurement in a. CB and VB represent the locations of the conduction band and the valence

band, respectively. \mathbf{c} , The T-dependent R_{xx} obtained on 04H-5QL at selected magnetic fields. The field is applied perpendicular to the film. \mathbf{d} , Out-of-plane upper critical field H_{c2} as a function of temperature. Solid lines are linear fits using the 2D Ginzburg–Landau model. Values of H_{c2} are read from the measurements shown in Supplementary Fig. 3f at fields where R_{xx} reaches 90%, 50% and 10% of the normal state resistance $R_{\rm n}$. The inset shows the optical image of 04H-5QL, where Ti/Au electrodes are directly deposited onto the film. Current source (I+), drain (I-), and high/low voltage (V+/-) probes are labelled. Scale bar, 5 μ m.

atomically sharp growth at every hetero-interface, as verified by cross-sectional scanning transmission electron microscopy (STEM; Fig. 1b). In addition, the strain effect induced by lattice mismatches between BST, epi-graphene and Ga is negligible, as the epi-graphene is quasi-freestanding upon Gaintercalation¹⁵, and the strain in MBE-grown Bi₂Te₃-family films is fully relaxed on a graphene substrate²⁰. The clean, van-der-Waals-like interface facilitates high-efficiency superconducting proximity coupling²². The grown film is transferred from the MBE chamber to an Ar-filled glove box without breaking vacuum. We construct a clean van der Waals tunnel junction consisting of a graphite electrode and a 1-2 layer hexagonal boron nitride (h-BN) tunnel barrier²³ (Fig. 1d) and transfer the tunnel junction to the BST/Gr/Ga film inside the glove box (Fig. 1c). The active area is encapsulated by a large h-BN sheet to prevent oxidization before the film is removed from the glove box and processed into a full device using lithography (Fig. 1e). Fabrication details are given in Supplementary Section 2. The use of a van der Waals tunnel junction preserves the pristine BST surface and enables measurements under a wide range of experimental conditions outside the growth chamber.

In situ angle-resolved photoemission spectroscopy (ARPES) measurements are performed on grown BST films to examine the film quality and Fermi level placement, $E_{\rm F}$. Figure 2a shows an exemplary band map of a 5 QL (Bi_{0.7}Sb_{0.3})₂Te₃/Gr/Ga film (Supplementary Fig. 1 for band maps on 8 and 10 QL films). The Dirac surface states are sharp and are the only states crossing the Fermi level, which fulfils the prerequisite for the formation of topological superconductivity. The ARPES band structure of films grown with the same chemical composition and thickness reproduces very well in different trials. The Dirac point is located at energy (E- $E_{\rm F}$) = -205 meV, which is roughly where the valence band maximum is. Guided by the ARPES results, we associate the occurrence of prominent slope changes on dI/dV spectra (I, current; V, voltage) taken on the same film with the onset of the bulk conduction and

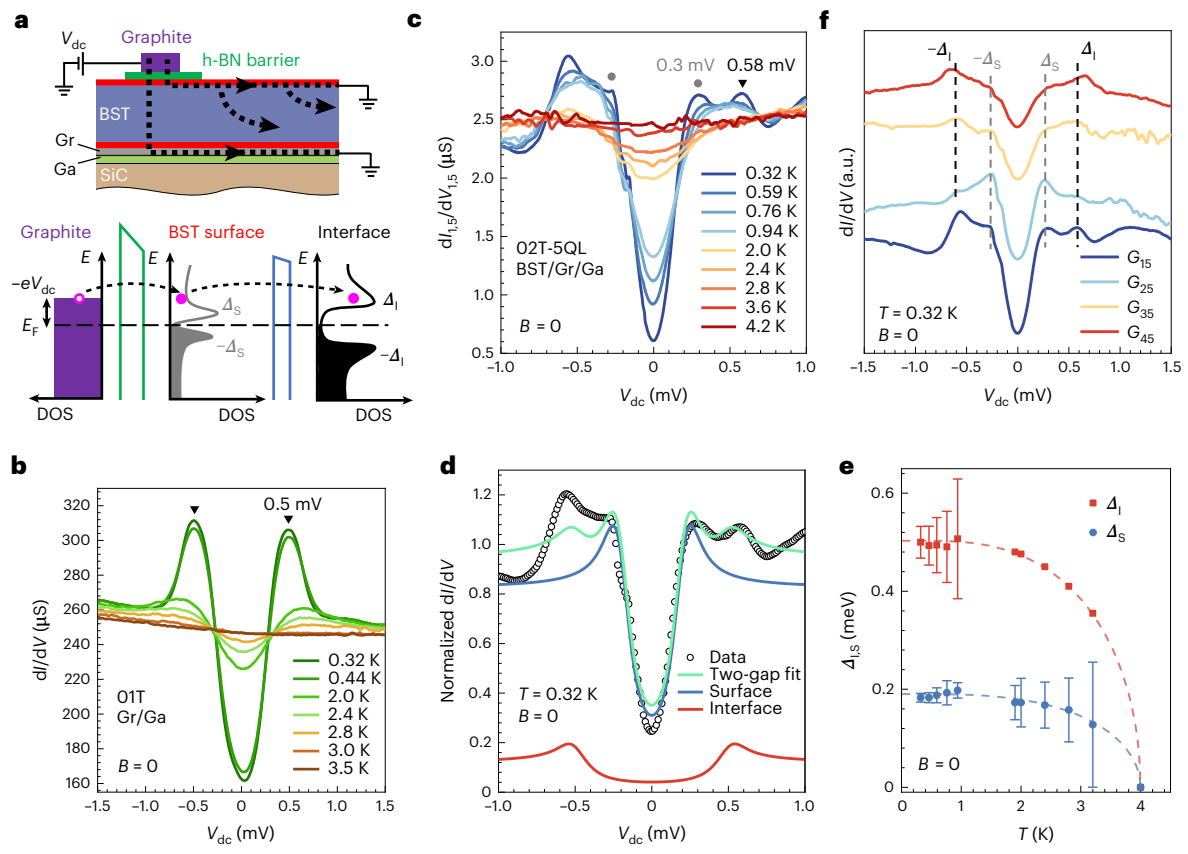


Fig. 3 | **Proximity-induced superconductivity in BST/Gr/Ga heterostructures. a**, Schematic of the two-gap tunnelling process and the corresponding density of states (DOS) diagrams. **b**, The dI/dV versus V_{dc} curves obtained on device 01T (Gr/Ga without the growth of BST) at selected temperatures. **c**, The dI/dV versus V_{dc} curves obtained on 02T-5QL between contacts 1 and 5 at selected temperatures. We examine the magnetic-field dependence of the spectra in Supplementary Fig. 5b to exclude coincidental features from the background, such as the sharp peak at $V_{dc} = -0.6$ mV. **d**, Fits to the 0.32 K data in **c** using a two-gap BTK model showing the contributions from the BST surface tunnelling (blue trace) and the BST/Gr/Ga interface tunnelling (red trace), as well as the total (green trace). The spectra weight of the blue trace is 88%. Only data at positive d.c. biases are fitted. **e**, The

 Δ_s and Δ_t versus temperature obtained from the best fits to the BTK model. The dashed lines plot the BCS temperature dependence of a SC gap given in equation (1) with a common T_c of 4 K. At $T \gtrsim 1.9$ K, we fix Δ_t following the red dashed line to obtain a more accurate fitting of Δ_s . Error bars represent 95% confidence interval of the fit. **f**, The dI/dV versus V_{dc} curves obtained on four different junctions G_{15} – G_{45} , where the two subscript numbers represent the contacts between which the conductance is measured, on 02T-SQL. Curves are normalized by their normal state conductance and stacked vertically for clarity. All curves show features associated with two SC gaps. Supplementary Figs. 4–6 show the full BTK analysis on Gr/Ga, 5 QL BST/Gr/Ga and 10 QL BST/Gr/Ga films.

valence bands, following prior studies in the literature 24,25 . The grey box in Fig. 2b corresponds roughly to the energy range of the bulk gap, consistent with the ARPES band map shown in Fig. 2a.

Owing to the epi-graphene reaction barrier, the growth of BST preserves the superconductivity of the 2 L Ga film¹⁵ extremely well. We perform temperature- and magnetic-field-dependent transport measurements on a series of heterostructures with varying BST film thickness. In these Hall bar devices, the metal electrodes contact the Gr/Ga film directly through occasional voids of the BST film (Supplementary Fig. 3b for cross-sectional STEM images of the electrode). Our results consistently show a critical temperature, T_c of 3-4.2 K and an upper critical perpendicular field H_{c2} of 50–80 mT for the Ga film. The variation of T_c among samples may be caused by the different number of Ga layers and the presence of superconducting weak links in the film. Figure 2c plots an example of longitudinal resistance R_{xx} versus temperature T measured on device 04H-5QL at selected fields. Here 04 is the film number as listed in Supplementary Table 1, H stands for Hall bar, and 5QL is the BST film thickness. Other devices are named following the same scheme. Additional data are given in Supplementary Section 3. Figure 2d plots H_{c2} versus T extracted from Supplementary Fig. 3f. The linear relationship between H_{c2} and T confirms the 2D

nature of the superconductivity²⁶. Our heterostructure film can support a critical current density J_c as large as 0.14 A μ m⁻² (Supplementary Fig. 3g), which is compared to other elemental superconductor films such as Al and Nb (ref. ²⁷).

Next, we perform tunnelling spectroscopy measurements on 5 QL and 10 QL BST/Gr/Ga films using devices similar to that shown in Fig. 1e. The construction and interfacial structure of the tunnel junction are described in detail in Supplementary Fig. 2. The tunnelling process is schematically illustrated in Fig. 3a. The tunnelling current can tunnel either (1) into the surface states of the BST film, and then flow to the drain electrode through a distributed network as shown in Fig. 3a, or (2) through the bulk to the Ga layer underneath; this allows us to probe the superconductivity of both layers. We have verified the efficacy of the van der Waals junction by first applying it to a Gr/Ga film, and the resulting dI/dV versus V_{dc} spectra are shown in Fig. 3b. Both the V-shaped dip near zero bias and the accompanying peaks at finite biases are characteristics of a superconducting gap, as observed in scanning tunnelling spectroscopy^{6,7,9} or point contact spectroscopy¹¹. Indeed, the tunnelling spectra in Fig. 3b can be well fit by a Blonder-Tinkham-Klapwijk (BTK) model²⁸, from which we obtain the temperature-dependent gap $\Delta(T)$, the tunnel barrier transparency Z and the lifetime broadening Γ of the

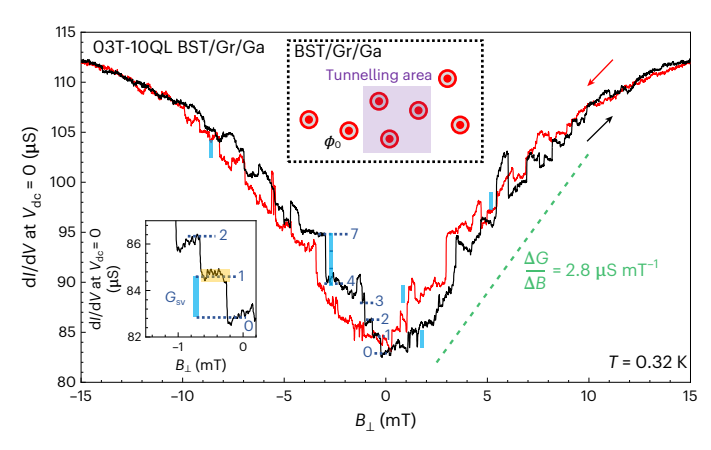


Fig. 4 | **Evidence of vortex trapping and single vortex signature in tunnelling conductance.** Zero-bias dI/dV measured on field upsweep (black trace) and downsweep (red trace) showing a vortex-induced conductance change, down to the effect of a single vortex. Sweep rate = $10 \, \mu T \, s^{-1}$. The lower inset expands on the black curve near B_\perp = 0. We attribute the smallest conductance step G_{sv} (vertical light blue in the inset) to the effect of a single vortex, G_{sv} = $1.7 \, \mu S$. The horizontal orange bar marks the noise level in our measurement. Conductance plateaus corresponding to the first few vortices are marked by dashed lines and labelled in the plot. The upper inset shows a schematic of Abrikosov vortices penetrating the tunnel junction area defined by the size of the graphite contact, $A \approx 3 \, \mu m^2$. The green dashed line is calculated from equation (2) using $A = 3.4 \, \mu m^2$ and agrees with the data very well. Data from junction J2 of O3T-10QL (see descriptions in Supplementary Section 5).

Cooper pairs (Supplementary Section 4 for details of the BTK model and fits to data). The $\Delta(T)$ is well described by the Bardeen–Cooper–Schrieffer (BCS) theory, i.e.

$$\Delta(T) = \Delta_0 \tanh\left(1.74\sqrt{\frac{T_c}{T} - 1}\right) \tag{1}$$

where $T_c = 3.1$ K is from transport studies of the same film and we obtain the zero-temperature gap $\Delta_0 = 0.395$ meV from the fits (Supplementary Fig. 4). The parameters of the Gr/Ga film serve as important references to the subsequent studies of BST/Gr/Ga films.

Figure 3c plots the T-dependent dI/dV versus V_{dc} curves obtained on device 02T-5QL, which is made on a 5 QL BST/Gr/Ga film. We observe the familiar V-shaped dip near zero d.c. bias and not one but two high-conductance humps at high biases. Both the dip and the humps weaken with increasing temperature and disappear completely above 4 K, which corresponds to the T_c of this film obtained in transport studies (Supplementary Fig. 3d). Not all features of the tunnelling spectra are related to superconductivity. We use the magnetic-field dependence of the spectra (Supplementary Fig. 5b for the junction shown in Fig. 3c) to identify accidental features coming from the background of the tunnel junction itself, for example, the sharp peak at $V_{\rm dc} = -0.6$ mV in Fig. 3c. Following the literature²⁹, we model the spectra as a weighted sum of two SC tunnelling processes. Exemplary fits to data using a two-gap BTK model are shown in Fig. 3d, from which we obtain and label the two gaps as Δ_S = 0.19 meV and Δ_I = 0.5 meV. Similar fits are obtained at other temperatures and the resulting $\Delta_s(T)$ and $\Delta_l(T)$ are plotted in Fig. 3e. Both $\Delta_s(T)$ and $\Delta_l(T)$ are well described by equation (1) with a common T_c of 4.0 K. These analyses strongly suggest that Δ_1 originates from the SC gap of the Ga film, while Δ_S is induced by the proximity effect.

Following previous scanning tunnelling microscopy studies on TI/SC heterostructures⁷⁹, we attribute Δ_s to the induced gap at the top

surface of the BST film, where the Dirac surface states reside, although future studies are needed to further clarify its origin. Single electron tunnelling into the BST film begins at $e|V_{dc}| \ge \Delta_s$, where the top surface turns normal; this gives rise to the zero-bias conductance dip and the first set of coherence peaks. At $e|V_{dc}| \ge \Delta_1$, a second tunnelling path opens, where an electron can reach the drain electrode through the bulk of the BST film and then the normal Ga film. This leads to the second set of coherence peaks. The fits in Fig. 3d illustrate the individual and the sum of the two tunnelling processes. The zero-bias conductance dip and the first coherence peaks are almost entirely given by Δ_s , making its value a very robust finding of the analysis. A proximity-induced SC gap is observed on four tunnel junctions made on film 02T-5QL (Fig. 3f), and our analysis gives Δ_s/Δ_t in the range of $37 \pm 4\%$ to $46 \pm 5\%$ (Supplementary Table 2), which is consistent with previous studies performed on Bi₂Se₃/NbSe₂ (refs. ^{6,11}), Bi₂Te₃/NbSe₂ (ref. 7) and Bi₂Se₃/Nb (ref. 30).

Similar measurements and analysis are performed on two tunnel junctions constructed on 03T-10QL BST/Gr/Ga films, producing Δ_s/Δ_1 in the range of $34\pm4\%$ to $42\pm2\%$. These measurements attest to the robustness of the proximity-induced superconductivity in the Dirac surface states of the TI film. A more complete and detailed analysis of the tunnelling spectra on 5 and 10 QL devices is given in Supplementary Section 5. In our set-up, tunnelling occurs over an area of approximately $3~\mu\text{m}^2$, where the thickness of the BST film could deviate from its nominal value by 1–2 QL. A more precise study of the dependence of Δ_s on film thickness $^{6.711,30}$ will require a different design.

In the remainder of the paper, we show a tunnelling conductance change due to the presence of Abrikosov vortices, which localize Majorana zero modes in a topological superconductor^{1,8}. A vortex is normal at its core, and its presence in the tunnelling area A raises the zero-bias tunnelling conductance by a certain amount $G_{\rm sv}$ (the upper inset of Fig. 4). If the number of vortices in the tunnel junction increases one by one by ramping an out-of-plane magnetic field B_{\perp} , we expect the zero-bias conductance G = dI/dV to increase from its zero-field value in a staircase pattern with an average slope of

$$\Delta G/\Delta B_{\perp} = \frac{A \times G_{\rm sv}}{\Phi_0} \tag{2}$$

where $\Phi_0 = h/2e$ is the magnetic flux quantum and h is the Planck constant. Figure 4 plots the measured zero-bias dI/dV versus B₁ on device 03T-10QL. While the general trend of the data agrees with equation (2), the change of conductance with B_{\perp} is not always monotonic, and the two field sweep directions show considerable hysteresis, suggesting the trapping of vortices. Furthermore, we observe conductance jumps in multiple integers of G_{sv} , suggesting that multiple vortices move together as a bundle³¹. Similar conductance jumps were observed in the transport tunnelling spectra on NbSe₂ when magnetic vortices appear or disappear from the tunnelling area³². The lower inset of Fig. 4 show examples of $\Delta G = 1G_{sv}$ and $\Delta G = 2G_{sv}$. The above characteristics are general to both Gr/Ga and BST/Gr/Ga junctions, with additional data given in Supplementary Section 6. These measurements show that transport tunnelling spectroscopy provides a valuable probe of the vortex dynamics, which can be performed concomitantly with current-phase studies in Josephson junctions to examine topological phase transitions and Majorana zero modes. These directions will be explored in future studies.

In summary, we demonstrate the growth and characterization of $(Bi,Sb)_2Te_3/Gr/Ga$ thin-film heterostructures, a potentially scalable platform that could be exploited to realize topological superconductivity. Using a clean van der Waals tunnel junction and transport tunnelling spectroscopy, we show experimental evidence of a robust proximity-induced superconducting gap in the Dirac surface states of the MBE-grown $(Bi,Sb)_2Te_3$ film and detect the presence of Abrikosov vortices in tunnelling conductance down to a single vortex. Our

synthetic approach of combining confinement heteroepitaxy and MBE opens the door to studies of novel superconducting and magnetic heterostructures. More sophisticated experiments and continued effort to improve the quality and uniformity of the heterostructure film are needed to advance the fundamental understanding and potential applications of topological superconductivity.

Online content

Any methods, additional references, Nature Portfolio reporting summaries, source data, extended data, supplementary information, acknowledgements, peer review information; details of author contributions and competing interests; and statements of data and code availability are available at https://doi.org/10.1038/s41563-023-01478-4.

References

- Fu, L. & Kane, C. L. Superconducting proximity effect and Majorana fermions at the surface of a topological insulator. *Phys. Rev. Lett.* 100, 096407 (2008).
- 2. Kitaev, A. Y. Fault-tolerant quantum computation by anyons. *Ann. Phys.* **303**, 2–30 (2003).
- Shabani, J. et al. Two-dimensional epitaxial superconductor-semiconductor heterostructures: a platform for topological superconducting networks. *Phys. Rev. B* 93, 155402 (2016).
- Frolov, S. M., Manfra, M. J. & Sau, J. D. Topological superconductivity in hybrid devices. *Nat. Phys.* 16, 718–724 (2020).
- Mourik, V. et al. Signatures of Majorana fermions in hybrid superconductor-semiconductor nanowire devices. Science 336, 1003–1007 (2012).
- Wang, M. X. et al. The coexistence of superconductivity and topological order in the Bi₂Se₃ thin films. Science 336, 52–55 (2012).
- Xu, J. P. et al. Artificial topological superconductor by the proximity effect. *Phys. Rev. Lett.* 112, 217001 (2014).
- Xu, J. P. et al. Experimental detection of a majorana mode in the core of a magnetic vortex inside a topological insulator-superconductor Bi₂Te₃/NbSe₂ heterostructure. *Phys. Rev. Lett.* **114**, 017001 (2015).
- Zang, Y. Y. et al. Competing energy scales in topological superconducting heterostructures. *Nano Lett.* 21, 2758–2765 (2021).
- 10. Zhang, H. et al. Two-step growth of high-quality Nb/ $(Bi_{0.5}Sb_{0.5})_2Te_3/Nb$ heterostructures for topological Josephson junctions. *J. Mater. Res.* **33**, 2423–2433 (2018).
- Dai, W. Q. et al. Proximity-effect-induced superconducting gap in topological surface states – a point contact spectroscopy study of NbSe₂/Bi₂Se₃ superconductor-topological Insulator heterostructures. Sci. Rep. 7, 7631 (2017).
- Williams, J. R. et al. Unconventional Josephson effect in hybrid superconductor-topological insulator devices. *Phys. Rev. Lett.* 109, 056803 (2012).
- 13. Kurter, C., Finck, A. D. K., Hor, Y. S. & Van Harlingen, D. J. Evidence for an anomalous current–phase relation in topological insulator Josephson junctions. *Nat. Commun.* **6**, 7130 (2015).
- 14. Kayyalha, M. et al. Anomalous low-temperature enhancement of supercurrent in topological-insulator nanoribbon Josephson junctions: evidence for low-energy Andreev bound states. *Phys. Rev. Lett.* **122**, 047003 (2019).
- Briggs, N. et al. Atomically thin half-van der Waals metals enabled by confinement heteroepitaxy. Nat. Mater. 19, 637–643 (2020).
- El-Sherif, H. et al. Scalable characterization of 2D gallium-intercalated epitaxial graphene. ACS Appl. Mater. Inter. 13, 55428–55439 (2021).

- Wetherington, M. T. et al. 2-dimensional polar metals: a low-frequency Raman scattering study. 2D Mater. 8, 041003 (2021).
- Gregory, W. D., Sheahen, T. P. & Cochran, J. Superconducting transition and critical field of pure gallium single crystals. *Phys. Rev.* 150, 315–321 (1966).
- Zhang, J. et al. Band structure engineering in (Bi_{1-x}Sb_x)₂Te₃ ternary topological insulators. Nat. Commun. 2, 574 (2011).
- Song, C. L. et al. Topological insulator Bi₂Se₃ thin films grown on double-layer graphene by molecular beam epitaxy. *Appl. Phys. Lett.* 97, 143118 (2010).
- Chang, C. Z. et al. Band engineering of Dirac surface states in topological-insulator-based van der Waals heterostructures. *Phys. Rev. Lett.* 115, 136801 (2015).
- 22. Li, J. et al. Superconducting proximity effect in a transparent van der Waals superconductor-metal junction. *Phys. Rev. B* **101**, 195405 (2020).
- 23. Bretheau, L. et al. Tunnelling spectroscopy of Andreev states in graphene. *Nat. Phys.* **13**, 756–760 (2017).
- Cascales, J. P. et al. Band structure of topological insulators from noise measurements in tunnel junctions. *Appl. Phys. Lett.* 107, 252402 (2015).
- Knispel, T. et al. Charge puddles in the bulk and on the surface of the topological insulator BiSbTeSe₂ studied by scanning tunneling microscopy and optical spectroscopy. *Phys. Rev. B* 96, 195135 (2017).
- 26. Cyrot, M. Ginzburg-Landau theory for superconductors. *Rep. Prog. Phys.* **36**, 103 (1973).
- 27. Talantsev, E. F., Crump, W. P. & Tallon, J. L. Universal scaling of the self-field critical current in superconductors: from sub-nanometre to millimetre size. *Sci. Rep.* **7**, 10010 (2017).
- Blonder, G. E., Tinkham, M. & Klapwijk, T. M. Transition from metallic to tunneling regimes in superconducting microconstrictions: excess current, charge imbalance, and supercurrent conversion. *Phys. Rev. B* 25, 4515–4532 (1982).
- Daghero, D. & Gonnelli, R. S. Probing multiband superconductivity by point-contact spectroscopy. Supercond. Sci. Technol. 23, 043001 (2010).
- 30. Flototto, D. et al. Superconducting pairing of topological surface states in bismuth selenide films on niobium. Sci. Adv. 4, eaar721 (2018).
- Suderow, H., Guillamon, I., Rodrigo, J. G. & Vieira, S. Imaging superconducting vortex cores and lattices with a scanning tunneling microscope. Supercond. Sci. Technol. 27, 063001 (2014).
- 32. Dvir, T., Aprili, M., Quay, C. H. L. & Steinberg, H. Tunneling into the vortex state of NbSe₂ with van der Waals junctions. *Nano Lett.* **18**, 7845–7850 (2018).
- Li, H. Y. et al. Electrode-free anodic oxidation nanolithography of low-dimensional materials. *Nano Lett.* 18, 8011–8015 (2018).

Publisher's note Springer Nature remains neutral with regard to jurisdictional claims in published maps and institutional affiliations.

Springer Nature or its licensor (e.g. a society or other partner) holds exclusive rights to this article under a publishing agreement with the author(s) or other rightsholder(s); author self-archiving of the accepted manuscript version of this article is solely governed by the terms of such publishing agreement and applicable law.

© The Author(s), under exclusive licence to Springer Nature Limited 2023

Methods

Confinement heteroepitaxy growth of 2D Ga

Gr/2D-Ga was grown using the CHet process described in ref. 15 . Briefly, silicon carbide (II-VI) was diced into 1×0.5 cm or 1×1 cm substrates and precleaned via a 20 minute soak in Nano-Strip (VWR, 90% sulfuric acid, 5% peroxymonosulfuric acid, <1% hydrogen peroxide). Subsequently, monolayer or bilayer epitaxial graphene was synthesized via silicon sublimation from the silicon carbide substrate for 20 minutes at 1,800 °C in a 700 torr argon atmosphere. Prior to intercalation, the graphene was subjected to an oxygen plasma (50 sccm He, 150 sccm O_2 at 500 mtorr and 50 W) in a M4L RF Gas Plasma system for 1 minute to generate defects that serve to facilitate metal diffusion to the graphene/SiC interface.

Intercalation was accomplished in a horizontal quartz tube (22 mm \times 25 mm, inner \times outer diameter) vacuum furnace, where gallium powder (Sigma-Aldrich, 99.99% trace metals basis, 30–100 mg) was placed in an alumina crucible directly below a downward facing, plasma-treated Gr/SiC substrate. Prior to heating, the tube furnace was evacuated and backfilled with ultra-high purity (UHP) Ar. Finally, the sample and Ga powder were heated to 800 °C for 30 minutes under a UHP Ar or forming gas (3% $\rm H_2$) environment at 300–700 torr, with 50 sccm total gas flow. The sample was then cooled to room temperature.

MBE growth of (Bi,Sb),Te,

 $(Bi,Sb)_2Te_3$ films were grown in a commercial MBE system (Omicron Lab 10) with a base vacuum of better than 2×10^{-10} mbar. Graphene/Ga/SiC substrates were outgassed at -350 °C for an hour prior to the growth of $(Bi,Sb)_2Te_3$. High purity Bi (99.9999%), Sb (99.9999%) and Te (99.9999%) were evaporated from Knudsen effusion cells. The flux ratio of Te per (Bi+Sb) was set to be greater than ten to prevent a tellurium deficiency in the film. The substrate was maintained at -230 °C during growth. The growth rate of the $(Bi,Sb)_2Te_3$ film was about 0.2 QL min⁻¹. Reflection high energy electron diffraction was used to monitor the growth. Grown films were annealed at -230 °C for 30 minutes to improve the crystal quality before cooling to room temperature. After in situ ARPES measurements, grown films were transferred to an argon-filled glove box using a small vacuum chamber to preserve the pristine $(Bi,Sb)_2Te_3$ surface.

In situ ARPES

ARPES measurements were performed in a chamber with a base vacuum of $^{-5}\times 10^{^{-11}}$ mbar. The MBE-grown $(Bi,Sb)_2Te_3$ films were transferred to the ARPES chamber without breaking the ultrahigh vacuum. The photoelectrons were excited by an unpolarized He-Ia light ($\sim\!21.2\,\text{eV}$), and a Scientia R3000 analyser was used for the ARPES measurements. The energy and angle resolutions are $\sim\!10$ meV and $\sim\!0.2^\circ$, respectively. All ARPES measurements were performed at room temperature.

Cross-sectional STEM

Cross-sectional transmission electron microscopy samples were prepared using FEI Helios 660 Nanolab and FEI Scios 2 focused ion beam systems. A thick protective amorphous carbon layer was deposited over the region of interest, and then Ga^{+} ions (30 kV, then stepped down to 1 kV to avoid ion beam damage to the sample surface) were used in the focused ion beam to make the samples electron transparent for transmission electron microscopy images. High-resolution STEM was performed at 300 kV on a dual spherical aberration-corrected FEI Titan 3 G2 60–300S/TEM instrument using a probe convergence angle of 24 mrad. The STEM images were collected using a high-angle annular dark-field detector with a collection angle of 50–300 mrad. Energy dispersive X-ray spectroscopy maps were acquired on an FEI Talos F200X S/TEM instrument operating at 200 kV.

Transport studies

All measurements were performed in a He-3 cryostat with a base temperature of 320 mK. We measured four-probe resistances using standard low-frequency lock-in techniques with an excitation current of 100 nA. To perform the differential conductance measurement, we applied a d.c. voltage with a small a.c. modulation of $10-50~\mu V$ to the graphite contacts and measured the a.c. current using a lock-in amplifier (Stanford Research SR860). To control the magnetic field finely, we used a Keithley 2400 sourcemeter to output current to the superconducting solenoid.

Data availability

The data needed to reproduce the figures in the main text and Supplementary Information are available on Zenodo (https://doi.org/10.5281/zenodo.7485214).

Code availability

The codes used in the theoretical simulations and calculations are available from the corresponding author upon reasonable request.

Acknowledgements

C.L., H.Y., C.-Z.C., S.K., T.B., J.L.T, J.A.R., D.R.H and J.Z. are supported by the Penn State Materials Research Science and Engineering Center for Nanoscale Science (DMR-2011839). Y.-F.Z, Z.Y. and C.-Z.C. are supported by the National Science Foundation CAREER award (DMR-1847811) and Gordon and Betty Moore Foundation's EPiQS Initiative (GBMF9063 to C.-Z.C.). C.D. and J.A.R. are supported by the Penn State National Science Foundation Materials Innovation Platforms Two-Dimensional Crystal Consortium award (DMR-1539916). A.V. and J.A.R. are supported by the National Science Foundation (DMR 2002651). O.L. and Y.O. are supported by the US-Israel Binational Science Foundation and National Science Foundation (2018643), the European Union's Horizon 2020 research and innovation programme (grant agreement LEGOTOP no. 788715), the DFG German Research Foundation (CRC/Transregio 183, EI 519/7-1) and ISF Quantum Science and Technology (2074/19). K. Watanabe and T.T. acknowledge support from the Japan Society for the Promotion of Science KAKENHI (grant numbers 19H05790, 20H00354 and 21H05233), J.L.T. and D.R.H. thank the Penn State Eberly College of Science. Department of Chemistry and Materials Research Institute for generous support through start-up funds. The coauthors acknowledge use of the Penn State Materials Characterization Lab. We thank C.-X. Liu, R. Mei and Y. Liu for helpful discussions and R. Zhang and F. Turker for assistance in measurement.

Author contributions

C.L. and J.Z. designed the experiment. C.L. fabricated the devices and made the transport measurements under the supervision of J.Z.; Y.-F.Z., H.Y. and Z.Y. performed the MBE growth and ARPES measurements under the supervision of C.-Z.C.; A.V., S.K., C.D. and T.B. performed the CHet growth and characterizations under the supervision of J.A.R.; O.L. performed BTK modelling under the supervision of Y.O.; K. Watanabe and T.T. synthesized the h-BN crystals; K. Wang, H.W. and J.L.T. under the supervision of D.R.H. performed the focused ion beam and transmission electron microscopy measurements; C.L. and J.Z. analysed the data; and C.L. and J.Z. wrote the manuscript with input from all authors.

Competing interests

The authors declare no competing interests.

Additional information

Supplementary information The online version contains supplementary material available at https://doi.org/10.1038/s41563-023-01478-4.

 $\begin{tabular}{ll} \textbf{Correspondence and requests for materials} should be addressed to \\ \textbf{Jun Zhu}. \end{tabular}$

Peer review information *Nature Materials* thanks the anonymous reviewers for their contribution to the peer review of this work.

Reprints and permissions information is available at www.nature.com/reprints.